Theory of optical anisotropy in quantum-well-wire arrays with two-dimensional quantum confinement

D. S. Citrin and Yia-Chung Chang
Department of Physics and Materials Research Laboratory, University of Illinois at Urbana-Champaign, 1110 West Green Street, Urbana, Illinois 61801
(Received 26 November 1990)

The effective bond-orbital model is used to calculate the conduction- and valence-subband structures of recently grown epitaxially buried GaAs/$Al_xGa_{1-x}As$/AlAs quantum-well-wire arrays. The model incorporates the coupling of the degenerate spin-$\frac{3}{2}$ valence bands and the *s*-like conduction bands. Band-structure parameters of all the materials involved are taken into account as well as the lateral intermixing of species, which has been observed in such structures. The quantum-wire (QWR) array is an intermediate case between quasi-one- and quasi-two-dimensional structures; the dispersion perpendicular to the QWR's is explainable in the combined terms of lateral confinement and zone folding. We calculate optical matrix elements within the model for light polarized parallel and perpendicular to the QWR's. When lateral intermixing is taken into account, the carriers occupy preferentially the nonmodulated part of the structure and exhibit only very weak optical anisotropy. Thus, the structure behaves like a two-dimensional rather than a one-dimensional system. We discuss our results in the context of the observed photoluminescence excitation spectra. It is found that band mixing, lateral diffusion, and the interplay of quasi-one- and quasi-two-dimensional properties play important roles in determining the electronic and optical properties.

I. INTRODUCTION

An important advance in the physics and engineering of ultrasmall structures is the ability to achieve quantum confinement of carriers in two dimensions without employing etching or lithography, as such techniques may provide a source for the introduction of defects. One approach to quantum-wire (QWR) fabrication is to utilize the different growth rates on the different crystal facets by deposition on patterned substrates. Epitaxially buried GaAs/$Al_xGa_{1-x}As$ QWR V-shaped grooves have recently been grown and the observation of lasing action in these structures has provided impetus for work in the field.[1] Another technique in nanostructure fabrication is the growth of epitaxially buried semiconductor quantum-wire arrays and tilted or vertical superlattices (SL) on vicinal substrates. While in conventional quantum wells (QW) and SL's the material interfaces parallel to growth planes provide the carrier confinement, in the QWR arrays and lateral SL's, a measure of control is gained over the motion of carriers in a lateral direction r_2 as well as in the growth direction x. This is achieved by modulating the material composition, and thus the band edges, in the lateral direction using a novel one-step growth process.[2] In this study we present theoretical calculations of the conduction and valence subbands and optical matrix elements of the QWR arrays grown by Tsuchiya *et al.*[2] The structure is a GaAs/$Al_{0.2}Ga_{0.8}As$/AlAs array of strongly coupled QWR's which shows characteristics of both one- and two-dimensional confinement. Photoluminescence excitation (PLE) spectra of this structure exhibits strong polarization dependence, the low-energy peak of which [labeled 1ehh in Fig. 2(b), Ref. 2] is stronger for parallel polarization than for perpendicular polarization. The situation is reversed for the second peak (that labeled 1elh in the abovementioned figure). In addition, we consider other similar structures in which the relative sizes of the features are varied.

Other workers have also measured optical anisotropy in a similar structure grown on a vicinal substrate.[3] The structure consisted of an array of antiwires (i.e., higher-band-gap material) centered in a QW. PLE data show only weak optical anisotropy. Because the antiwires sample the maxima of the relevant envelope functions involved in the optical transitions, this setup is ideal to examine how an array of lateral barriers perturbs QW states. For the structure of Ref. 2, however, the lateral barriers are at the edge of the well where the amplitudes of the envelope functions are small. Thus we would expect the optical anisotropy to be rather weak. Of course, this assumes that the correct picture is of a QW perturbed by a lateral modulation. In the sequel we shall show that this picture is born out by detailed calculations.

Several theoretical accounts of optical anisotropy in structures of reduced dimensionality have recently appeared in the literature. Reference 2 contains a theoretical description of polarization dependence of the heavy-hole and light-hole excitons for a QWR of square cross section. As pointed out by Sercel and Vahala,[4] however, the agreement is fortuitous; the treatment in Ref. 2 neglects the band mixing and quantum-mechanical coherence effects. It is shown that, when the latter are included, the one-band model predicts no optical anisotropy. Sercel and Vahala drive the zone-center optical anisotropy of the squared optical matrix elements in a coupled-band model in the axial approximation for a cy-

lindrical QWR:

$$\frac{|\hat{\epsilon}\cdot\mathbf{P}_{1e,1h}(0,0)|^2}{|\hat{\epsilon}\cdot\mathbf{P}_{1e,2h}(0,0)|^2}=\frac{\frac{1}{2}\sin^2\theta I_{1e,1h}^2}{(\frac{2}{3}\cos^2\theta+\frac{1}{6}\sin^2\theta)I_{1e,2h}^2},$$

where $\hat{\epsilon}$ is the polarization vector making angle θ with the QWR axis, $1h$ and $2h$ denote the first and second valence subbands, and I is the overlap integral. This expression gives the ratio of the strengths of the zone center $1e$-$1h$ and $1e$-$2h$ transitions at the center of the Brillouin zone and also approximately gives the ratio of the oscillator strengths for the corresponding excitonic transitions. Another comment on the one-band model is that assumption of heavy-hole and light-hole states in a QWR is inconsistent because the irreducible representations for the hole states in a QWR transform neither like the heavy hole nor the light hole but have mixed heavy-hole–light-hole character at all k in contrast to a QW where the states are decoupled at the zone center. The group theoretical treatment of QWR valence-band states for QWR's of square cross section is discussed in Refs. 10 and 6. Apart from any discussion of the correct treatment of optical anisotropy in QWR's, it is important when discussing real structures to begin with an unbiased theory, i.e., one that does not make *a priori* assumptions about the lateral confinement. The present study represents such an effort. We shall see that the QWR array has optical properties intermediate between those predicted for a pure QWR and a QW.

Our theoretical results for this structure are summarized as follows. A detailed treatment including band mixing, the actual geometry of the structure, and lateral intermixing of the constituent atomic species across lateral interfaces necessarily must be undertaken as the energy-level spacings as well as the strengths of the optical transitions are found to depend sensitively on these factors. We find that the subband dispersion in the direction of the QWR's r_1 is intermediate between that previously calculated for other QWR structures[5–12] and for QW's. The dispersion perpendicular to the QWR's but in the plane of the array is non-negligible indicating that the fabricated structure cannot be considered simply as an array of *uncoupled* QWR's. The interplay of zone folding together with lateral confinement qualitatively explains the subband dispersion. The details of the subbands often referred to as light-hole (lh) depend sensitively on lateral intermixing and the particulars of the geometry; the heavy-hole (hh) subbands are less sensitive to these effects. We also calculate optical matrix elements for light polarized along the QWR's and perpendicular to the QWR's but in the plane of the array. Although our results are in qualitative agreement with experiment, we are unable to obtain close quantitative agreement between theory and the observed polarization-dependent PLE spectra. Based on our calculations, we expect the structure of Ref. 2 to display weak, if not negligible, optical anisotropy. In Sec. II we discuss our theoretical methods, and in Sec. III we present the results for the sub-band dispersion and optical matrix elements for the QWR array of Ref. 2 and compare our results with the experimental data. The electronic structure at the center of the Brillouin zone is investigated for related QWR arrays in Sec. IV. Section V concludes this paper.

II. THEORETICAL METHOD

The effective bond-orbital model (EBOM)[13] employed here is a tight-binding-like model which includes nearest-neighbor interactions among bond orbital residing on an fcc lattice. Although it possess symmetry higher than that of a zinc-blende crystal, it captures the salient features of the electronic structure. In particular, the polar character of the crystal, which gives rise to terms in the Hamiltonian linear in k, is neglected. The version of the EBOM used in these calculations describes the coupling between the upper four spin-$\frac{3}{2}$ valence bands and the lowest two s-like conduction bands. For the GaAs/AlGaAs system the band-edge properties are relatively uneffected by the split-off band[10] since the spin-orbit splitting is large ($\Delta=340$ meV). Thus, we assume $\Delta=\infty$ which decouples the split-off bands from the problem. A bond orbital is defined to be the proper linear combination of two atomic orbitals within a zinc-blende crystal which best describes the states near the center of the Brillouin zone. The parameters that appear in the theory are given by a correspondence with the effective-mass parameters. This correspondence is made by requiring that the Hamiltonian in the bond-orbital basis, when written for the bulk material and expanded to second order in k, agree with the Luttinger-Kohn expression. For interactions across heterojunctions, we take the average of the matrix elements for the two bulk materials. The matrix elements across the interface alternatively can be considered as adjustable parameters with the requirement that the theoretical band structures agree with the experimental data. We have found, using QW, that the averaging procedure produces results in good agreement with other methods. In any case, because the magnitude of the wave function is small at the GaAs-$Al_xGa_{1-x}As$ interfaces for the cases in which we are most interested, the exact values of the interaction parameters between materials is not of critical importance. The model includes the anisotropy of the effective-mass parameters, the nonparabolicity, the different band-structure parameters of all participating materials, and treats the interfaces in a realistic and straightforward manner. Furthermore, EBOM's tight-binding-like nature allows the unprecidented rigorous treatment of the complicated geometries of structures that are actually fabricated. EBOM has recently been used to calculate the valence- and conduction-subband structure of epitaxially buried $In_xGa_{1-x}As$/InP QWR of triangular cross section.[12,14] For a detailed account of the general theory of EBOM, see Ref. 13.

Our treatment of the QWR proceeds as follows.[12] We first calculate the band structure of a SL with M bilayers in the well material and N bilayers in the barrier material using the slab method. The well thickness is $L_\perp=L_\perp^B+L_\perp^W=Ma/2$ where a is the lattice constant. For a sufficiently large value of the barrier thickness (we use $L_\perp=204$ Å) the QW's are essentially decoupled and we ignore the dependence on the wave number in the

growth direction, taking $q=0$. The SL eigenstates with $q=0$ are denoted by $|k_1,\bar{k}_2,n\rangle$ where k_1 is the wave number in the QWR (i.e., r_1) direction, $\bar{k}_2$ is the wave number perpendicular to the QWR axis but in the plane of the SL (i.e., r_2 direction), and n is the subband index. The wave number k_1 is a good quantum number for the QWR array. The QWR wave function is a linear combination of SL wave functions with the same k_1 but with values of $\bar{k}_2$ differing by $2\pi/L_2$ where L_2 is the periodicity of the array of QWR's in the r_2 direction. We define k_2 to be the wave number of the QWR array in the r_2 direction, and we can write $\bar{k}_2=k_2+2\pi\zeta/L_2$ with $\zeta=0,1,2,\ldots,m$ where $m=L_2/a_2$ with $a_2=a$ for $\hat{\mathbf{r}}_2\|\langle 001\rangle$ and $a_2=a/\sqrt{2}$ for $\hat{\mathbf{r}}_2\|\langle 011\rangle$. The QWR Hamiltonian is then diagonalized in the basis $|k_1,k_2+2\pi\zeta/L_2,n\rangle$ of SL eigenstates with k_1 and k_2 fixed. The basis is suitably truncated in ζ and n in order to yield a matrix diagonalization problem of manageable size while insuring satisfactory convergence of the subband energies. Because the basis is truncated, the calculation is of a variational nature. Although the subbands closest to the band edge are converged to within 0.1 meV, other subbands may not be so accurate. The power of this approach lies in the truncation. The problem that begins with a Hamiltonian matrix the size of which is given by the number of sites in a QWR supercell times the number of coupled bands is reduced in size to the number of SL states necessary to give accurate results for the QWR. In practice, this number is ~ 200 in order that the two uppermost pair of valence subbands are well converged. In this study, however, we use ~ 600 basis elements in order to ensure the accuracy of the deeper lying states for all calculations and figures (except for Figs. 3 and 7 which are included for illustrative purposes) in this paper.

For large M and N the computation becomes lengthy. For such cases we employ the a scaling approximation.[15] To calculate the subband structure of a QWR with $M'=sM$, we calculate the subbands for a QWR with thickness M but with the material parameters replaced by s^2E_g, s^2V_0, and s^2V_c where E_g is the band gap and V_0 and V_c are the band offsets in the valence and conduction bands. The desired subband structure is then given by $E_n(k_1/s,k_2/s)/s^2$ for the scaled QWR. This is equivalent to using a bond-orbital model with enlarged unit cells. For the calculations in this study, $s=2$ and $N=36$. The effect of lateral intermixing of the Al and Ga is accounted for using the virtual-crystal approximation. Bond-orbital parameters for the interdiffused materials are obtained by linearly interpolating between the values of the parameters for the pure materials. The particular profile we explore for the lateral modulation in the composition are discussed below in Sec. III. Apart from the additional complications of lateral dispersion and intermixing, our method for obtaining the subband structure can be perused in Ref. 12.

To calculate optical matrix elements between QWR states, we need to know the optical matrix elements between any two bond orbitals. Using symmetry considerations, we can write down the expressions for the optical matrix elements between bond orbitals. The optical parameters in these expressions are determined by requiring that the optical matrix elements between bulk states obtained by EBOM be identical to those obtained in the $\mathbf{k}\cdot\mathbf{p}$ theory up to second order in $\mathbf{k}$ (Ref. 16). We outline the method[17] by which EBOM expressions for the optical matrix elements are found. In the bulk material, the optical matrix element between a bond orbital of symmetry type α at the origin and another bond orbital of type α' located at position τ is

$$P^{\beta}_{\alpha\alpha'}(\tau)=-i\hbar\left[\frac{2}{m_e}\right]^{1/2}\int d^3r\,\phi_{\alpha}(\mathbf{r})\frac{\partial}{\partial\beta}\phi_{\alpha'}(\mathbf{r}-\tau)\ . \tag{1}$$

Here $\alpha=s,x,y,z$ and $\beta=x,y,z$ is the polarization of the incident photon. By keeping only the leading contributions and by exploiting the symmetry, we obtain the following relations:

$$P^{\beta}_{s\alpha}(\tau)=-P^{\beta}_{\alpha s}(\tau)=iQ_{sp}\delta_{\alpha\beta},\quad \alpha=x,y,z\ , \tag{2}$$

for $\tau=0$ and

$$P^{\beta}_{ss}(\tau)=iP_{ss}\tau_{\beta}\ , \tag{3}$$

$$P^{\beta}_{\alpha\alpha'}(\tau)=iP_0\tau_{\alpha}\tau_{\beta}\tau_{\alpha'}+iP_1\delta_{\alpha\alpha'}\tau_{\beta}+iP_2(\delta_{\alpha'\beta}\tau_{\alpha}+\delta_{\alpha\beta}\tau_{\alpha'}),\quad \alpha,\alpha'=x,y,z\ , \tag{4}$$

for $\tau=\sqrt{2}$ where τ is measured in units of $a/2$ and τ_{α} is the αth component of τ. The other optical matrix elements are neglected. The five parameters Q_{sp}, P_{ss}, P_0, P_1, and P_2 can be related to the $\mathbf{k}\cdot\mathbf{p}$ parameters by requiring that the optical matrix elements between bulk states obtained by EBOM be identical to those obtained in the $\mathbf{k}\cdot\mathbf{p}$ theory.[17] One finds $Q_{sp}=\sqrt{E_p}$, $P_{ss}=(\lambda-m_0/m_c^*)R_0$, $P_0=24(\gamma_3-\gamma_2)R_0$, $P_1=(\gamma_1+5\gamma_2-6\gamma_3)R_0$, and $P_2=(6\gamma_2-3\gamma_3-\lambda/2)R_0$ where $\gamma_1,\gamma_2,\gamma_3$ are Luttinger parameters, $E_p=(2/m_0)|\langle s|p_x|x\rangle|^2$, $R_0=[\hbar^2/(4m_0a^2)]^{1/2}$, and $\lambda=E_p/E_g$. Using the bulk expressions for optical matrix elements together with the eigenstates, the optical matrix elements for QWR are calculated. In the following, we use GaAs optical matrix elements throughout the supercell in order to reduce computation time. Because the elementary optical matrix elements for AlGaAs differ little from those for GaAs, and since the magnitude of the wave function is, in any case, small in the barrier material, this is a good approximation.

III. RESULTS

In this section we present and discuss our results for the electronic structure and optical matrix elements for QWR arrays such as those grown in Ref. 2. We begin by neglecting the lateral intermixing that smears interfaces perpendicular to the growth direction in such structures. Later, we introduce lateral intermixing into the calculations and show that it has a strong effect on the electronic and optical properties, particularly of those features involving sizable lh contributions.

In Fig. 1 is sketched a cross section of the QWR array grown by molecular-beam epitaxy (MBE) in Ref. 2. The array is grown on a vicinal (100) GaAs substrate with a tilt of 2° in the [011] direction. Associated with this tilt are monolayer steps alined with $[0\bar{1}1]$ spaced an average

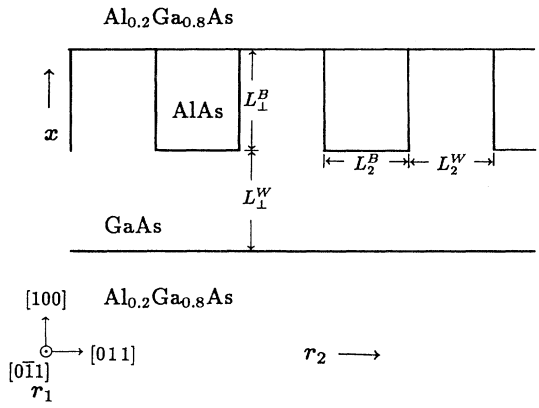

FIG. 1. QWR array such as is fabricated in Ref. 1. The QWR axis lies in the [011] direction. The lateral period is $L_2 = L_2^B + L_2^W$.

of 80 Å apart. Similar metal-organic-chemical-vapor-deposition (MOCVD) -grown structures have the monolayer steps alined with the [0$\bar{1}$1] direction. As EBOM does not make this distinction (it treats an fcc lattice), our calculations apply to both the MBE- and MOCVD-grown QWR arrays. Structures with other tilt angles and corresponding step lengths have also been fabricated (see below in Sec. IV). By successively depositing submonolayers of GaAs and AlAs on the tilted substrate, one attempts to grow the desired structure. The QWR array shown is a special case of a tilted SL.[18,19] The structure has its axis along the [011] and incorporates the three materials GaAs, $Al_{0.2}Ga_{0.8}As$, and AlAs. The carriers are confined to the GaAs region. The material parameters used in our calculation are given in Table I. All energies are measured with respect to the valence-band edge of bulk GaAs. Our calculations neglect the 2° tilt. Studies have found that the interfaces normal to the r_2 direction (henceforth referred to as lateral interfaces) and rather ill defined[24–26] due to the lateral migration of Ga and Al during growth. We include this lateral intermixing in our treatment later in this section.

Before we discuss the physical implications of our results, a few words on the accuracy of our method are in order. Using EBOM, we calculated the subband structure of the QW shown in Fig. 2(a) of Ref. 2. We find the 1e-1hh and 1e-1lh transitions to be 1585 and 1602 meV, respectively, neglecting excitons. Taking excitons into account further reduces these values by about 10 meV.[27] These results disagree with the spectra of Ref. 2 which shows peaks at 1602 meV (1e-1hh) and 1625 meV (1e-1lh). We find, however, that our model is in good agreement with other experimental[28] and theoretical data.[29] (See Table II for a comparison with Ref. 29.) We conclude that uncertainty exists in the parameters given in Refs. 2—Al concentration may be higher than quoted ($x=0.2$) or the well may be narrower than the value given ($L_\perp=6$ nm). Similarly, for the spectra of Fig. 2(b) of Ref. 2, our calculation underestimates the energy of the transitions by a comparable amount. A recent study of similar tilted SL's indicates that the period in the r_2 direction may vary between 65 and 110 Å.[24] We shall have more to say about this variation in the period below where we investigate the subband structure as a function of the parameters L_2^B and $L_\perp^B$ in Sec. IV. Furthermore, our calculations for QWR's of rectangular cross section calculated using EBOM are in agreement with previous results we obtained in the effective-mass approximation.[10,12]

For the sake of clarifying the different physical effects due to confinement, we begin with calculations of the subband dispersion in which the lateral interfaces are assumed to be atomically sharp. This situation refers to the nominal structure as sketched in Fig. 1. Later we consider the effects of lateral intermixing.

A. Subband dispersion

The calculated subband structure for the QWR array shown in Fig. 1 is given in Fig. 2 (solid curves). The conduction subbands (not shown in the figure) are approximately parabolic near the Γ point. The subband splitting at $k\neq 0$ is spin splitting due to the lack of inversion symmetry of the structure. The first conduction subband 1e is at 1592 meV at the Γ point. This gives the energy gap of 1610 meV for the QWR array. (The first PLE peak 1e-1hh is observed at 1624 meV.) The calculated conduction subbands were used to obtain the effective masses.

TABLE I. Material parameters used in calculations in this study. The valence-band offsets V_0 are with respect to the bulk-valence-band edge of GaAs. $T=4.2$ K.

Materials	γ_1	γ_2	γ_3	m_e^*/m_e	$E_g(\Gamma)$ (meV)	V_0 (meV)
GaAs[a]	6.85	2.1	2.9	0.0665	1.5177	0
$Al_{0.2}Ga_{0.8}As$[b]	6.01	1.57	2.5	0.0831	1.7635	0.076[c]
$Al_{0.5}Ga_{0.5}As$[b]	5.08	1.14	2.04	0.108	2.1877	0.067[c]
AlAs[a]	4.04	0.78	1.57	0.12	3.13	0.43[d]

[a]From Ref. 20.
[b]Effective masses and energy gaps obtained by linear interpolation between the end-point materials from Ref. 16. Inverses of Luttinger parameters for the alloy are obtained by linear interpolation of reciprocal Luttinger parameters from Ref. 16. We ignore the indirect nature of $Al_{0.5}Ga_{0.5}As$.
[c]From Refs. 21 and 22.
[d]From Ref. 23.

TABLE II. Transition energies in meV for the 67 Å/175 Å $GaAs/Al_{0.36}Ga_{0.64}As$ superlattice calculated by the pseudopotential method and by EBOM.

Transition	Pseudopotential[a]	EBOM
1*e*-1hh	1585	1589
1*e*-1lh	1607	1611
1*e*-3hh	1685	1693
2*e*-1lh	1752	1758
2*e*-2hh	1773	1774
2*e*-3lh	1830	1837
2*e*-2lh	1845	1856

[a]From Ref. 25.

TABLE III. Percent hh character for pairs of valence subbands at the Γ point and at the minizone boundary $k_2=\pi/L_2(k_1=0)$ for the ideal case of no lateral intermixing. 1hh and 1lh label the subbands as referred to in the text.

Subband	% heavy hole			
	$\nu=0$		$\eta=1$	
	$k_2=0$	π/L_2	0	π/L_2
1	94(1hh)	34	100(1hh)	57
2	25(1lh)	44	42	58
3	44	45	44	61
4	44	47	42	65
5	44	46	9(1lh)	57
6	45	44	45	65
7	34	46	57	39

This was accomplished by fitting the subbands near the Γ point to a polynomial. The effective masses of 1*e* are $0.074m_e$ in the r_1 direction and $0.081m_e$ in the r_2 direction. The value of the effective masses are somewhat higher than the bulk value ($m_e^*=0.0665m_e$).

Unlike for the QW, the zone-center states for the QWR already contain an admixture of both hh and lh.[8] The percent hh character of the pairs of states at the Γ point is given in Table III. The uppermost valence subband 1hh is 94% hh at the Γ point. Deeper subbands show stronger mixing. Nevertheless, we shall conform with custom and refer to the QWR subbands as 1hh and 1lh as labeled in Table III. We must bear in mind, however, that this appellation is not strictly correct.

Referring again to Fig. 2 for dispersion in both the r_1 and r_2 directions, we observe strong interaction between the subbands. Minigaps open at $k_2=\pi/L_2$. The uppermost pair of subbands, 1hh, has somewhat flattened dispersion in the k_2 direction compared with the dispersion for a 50-Å asymmetric QW (dashed curves) or with the QWR dispersion in the r_1 direction. (The 50-Å asymmetric QW is $Al_{0.5}Ga_{0.5}As/GaAs/Al_{0.2}Ga_{0.8}As$ in order to account for the mean composition in the modulated layer.) The second pair of subbands, 1lh, is quite aniso-

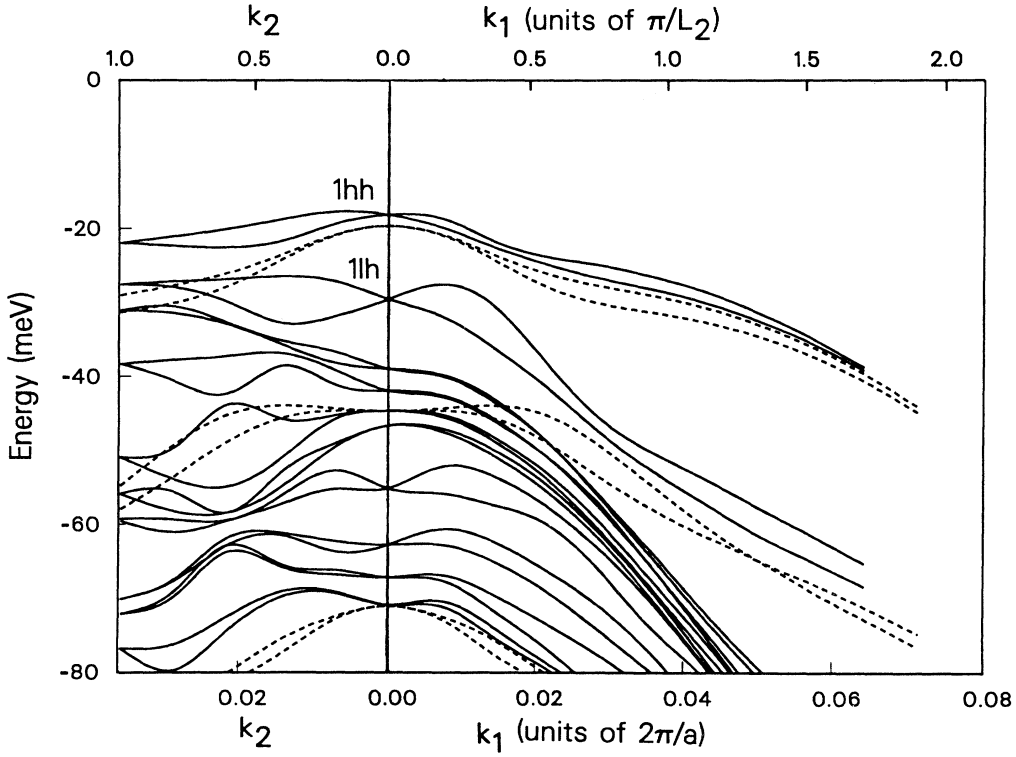

FIG. 2. Valence-subband dispersion (solid curves) in the k_2 and k_1 directions for the structure illustrated in Fig. 1 with perfect lateral interfaces. $L_1^W=L_1^B=50$ Å, $L_2^W=L_2^B=40$ Å. Dashed curves show valence-subband dispersion for a 50-Å $Al_{0.5}Ga_{0.5}As/GaAs/Al_{0.2}Ga_{0.8}As$ quantum well. Energies are measured from the bulk GaAs valence-band edge.

tropic. A zone-folding scheme explains some of the apparent anisotropy in the subband dispersion. In Fig. 3 is shown the valence-subband dispersion of Fig. 2 in both the r_1 (dashed curves) and r_2 (solid curves) directions. (The small discrepancies between Figs. 3 and 2 are due to the more severe truncation of the basis used to obtain Fig. 3.) The dispersion for the r_1 direction has been folded over into the minizone measured in the r_2 direction. It is immediately evident that many of the subbands in the r_2 direction are closely approximated by the folded subbands in the r_1 direction. Several of the anticrossings between the subbands in the r_2 direction are seen to be associated with crossings that occur for folded r_1 subbands. Other features, however, cannot be explained in terms of the folded-zone scheme. The first and second pair of valence subbands, 1hh and 1lh, in particular display effects of lateral confinement. As already pointed out, the 1hh subband shows some flattening in the r_2 direction. For the second pair of subbands $h2$ the behavior is more complicated. The first subband of the pair is quite flat over the entire range of k_2 indicating very strong quasi-two-dimensional confinement. The second subband of the pair is isotropic for $k_2 < 0.012(2\pi/a)$ but for greater values of k_2 follows the first pair of folded valence subbands in the r_1 direction.

The dashed curves in Fig. 2 are the subbands for a 50-Å $Al_{0.5}Ga_{0.5}As/GaAs/Al_{0.2}Ga_{0.8}As$ asymmetric QW. The QWR subband structure is seen to depart from the QW dispersion especially for the 1lh subband. In the next paragraph we shall see that the flattening of the 1lh subband and the more isotropic behavior of the 1hh subband are reflected in the probability densities of the states at the zone center.

It is instructive to plot the probability densities of a few states near the band edges in order to see the effects of two-dimensional confinement. In Figs. 4–6 are plotted probability densities in the (011) plane for the first pair of conduction subbands $1e$ and the first two pairs of valence subbands 1hh and 1lh, respectively. Figures 4(a), 5(a), and 6(a) show the probability densities at the center of the Brillouin zone while Figs. 4(b), 5(b), and 6(b) show the charge densities at the minizone boundary, $k_1=0$ and $k_2=\pi/L_2$. (Degenerate states have the same probability densities.) The AlAs barriers lie in the regions bounded by $|x-9|\leq 9$ and $|r_2-5|\leq 5$ in units of a. The $Al_{0.2}Ga_{0.8}As$ layers are $|x-9|>9$. Figures 4(a) and 5(a) show $1e$ and 1hh, the conduction and valence states closest to the respective band edges. The quasi-two-dimensional confinement appears to be small; rather, the charge densities appear overall to be characteristic of a QW. The first valence subband, recall, is predominantly of hh character (94%) at the center of the Brillouin zone. The QWR potential induces only a small amount of band mixing for this state. Still, there is sufficient lateral confinement to give rise to significant optical anisotropy (see Sec. III B). In Fig. 6(c) is plotted the probability density of the zone-center state for the 1lh. Quasi-two-dimensional confinement effects are seen to be much stronger than for the 1hh. There is, however, significant coupling between the QWR's. That the lh experiences the strongest lateral confinement on the surface appears to go against the fact that in bulk the effective masses of the electron, the lh, and the hh are increasing in that order. This difficulty is merely apparent and can be understood by considering the QWR array as a perturbed 50-Å QW. In this case, the lh in-plane effective mass exceeds that of the hh. The addition, then, of the lateral modulation in the band gap is most effective in confining the lh's. We also include plots of the probability densities of the same subbands at the minizone boundary in the r_2 direction. We can see that 1hh experiences considerable lateral confinement while 1lh is confined primarily in the layer $L_\perp^W$ thick. This switch in character is a consequence of the strong band mixing and the anticrossing that occurs between the 1hh and 1lh subbands at $k_2 \sim 0.5(\pi/L_2)$. At $k_2=\pi/L_2$, 1lh has more hh character than 1hh (see Table III). On the basis of the probability densities and the subband structure we can expect therefore the effects of quasi-two-dimensional confinement to be strong for features associated with the 1hh and 1lh subbands.

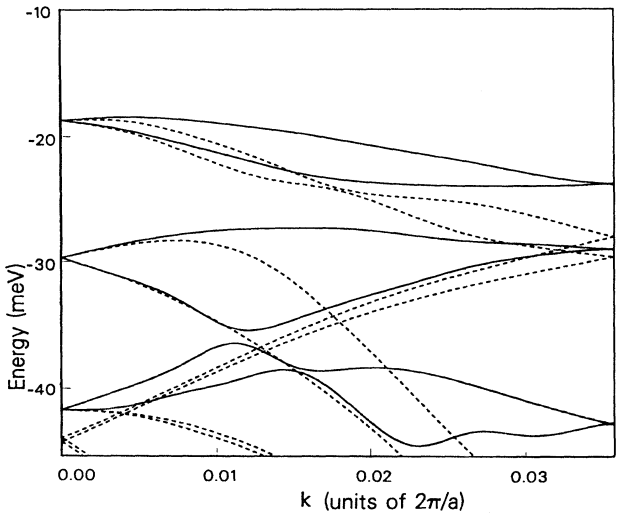

FIG. 3. Valence subbands of Fig. 2. The k_1 subbands (dashed) are folded into the k_2 minizone. k_2 subbands are given by the solid curves.

The subband calculations include the anisotropy of the effective-mass parameters. It is of interest to see the effect the anisotropy of the effective-mass parameters have on the QWR subband structure since the axial and spherical approximations have been used in several previous calculations.[8–11] In Fig. 7 is plotted the subband structure of a QWR array of the same nominal geometry as the grown structure but with the QWR axes lying along the [001]. Although the confinement energy for the 1hh subband is approximately the same as for the QWR's lying along the [011], the 1lh subband is quite different. The conduction subbands in the two cases, though, are similar. The discrepancies between Figs. 2 and 7 give a measure of the inadequacy of the axial and spherical approximations for the lh subbands. QWR states with small k_1 have appreciable admixtures of QW states of

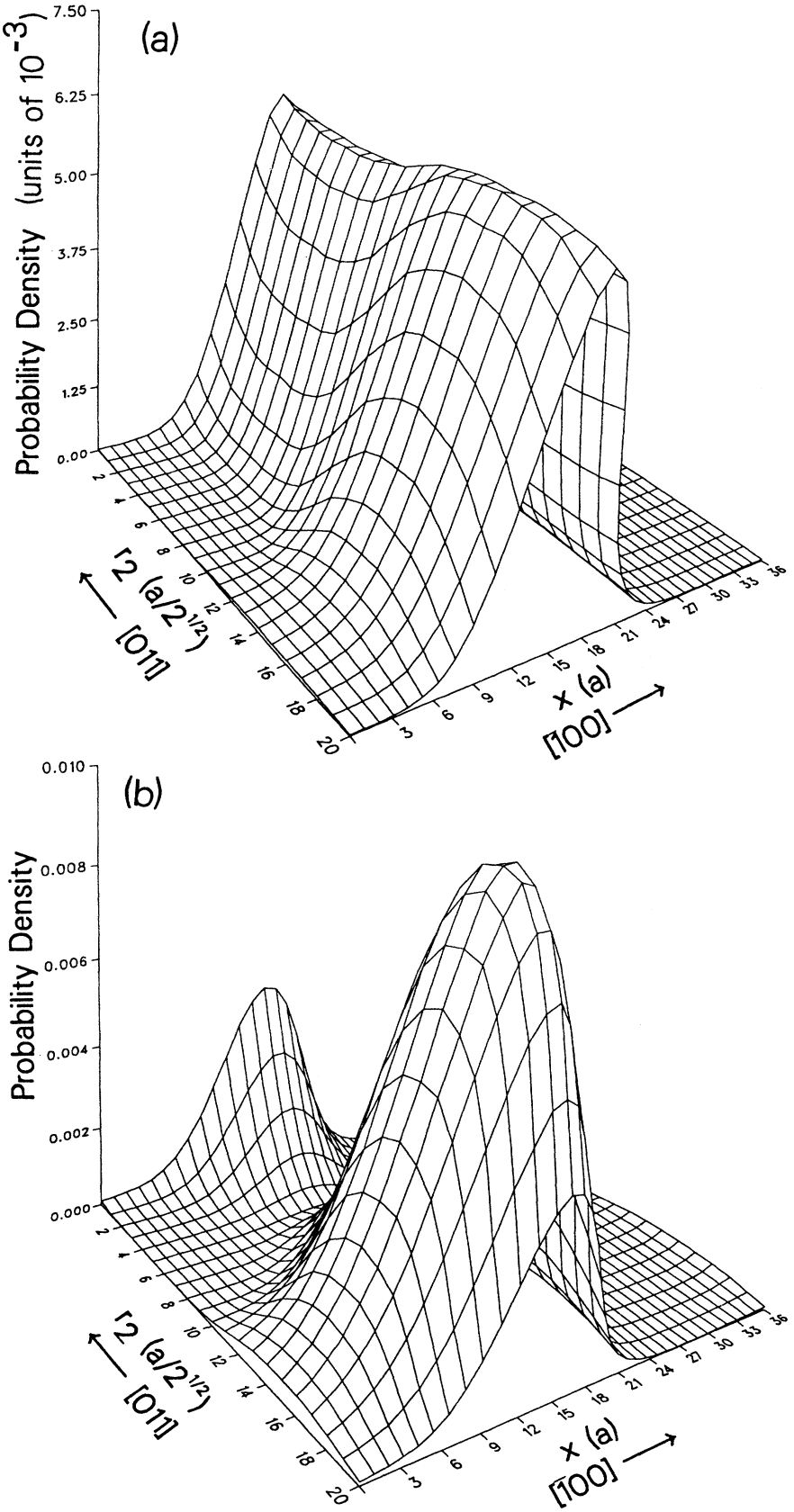

FIG. 4. Probability density plotted within the QWR supercell of the state at (a) the zone center and (b) at the minizone boundary ($k_1=0, k_2=\pi/L_2$) for the first pair of conduction subbands (1e) for the QWR array with parameters used for Fig. 2.

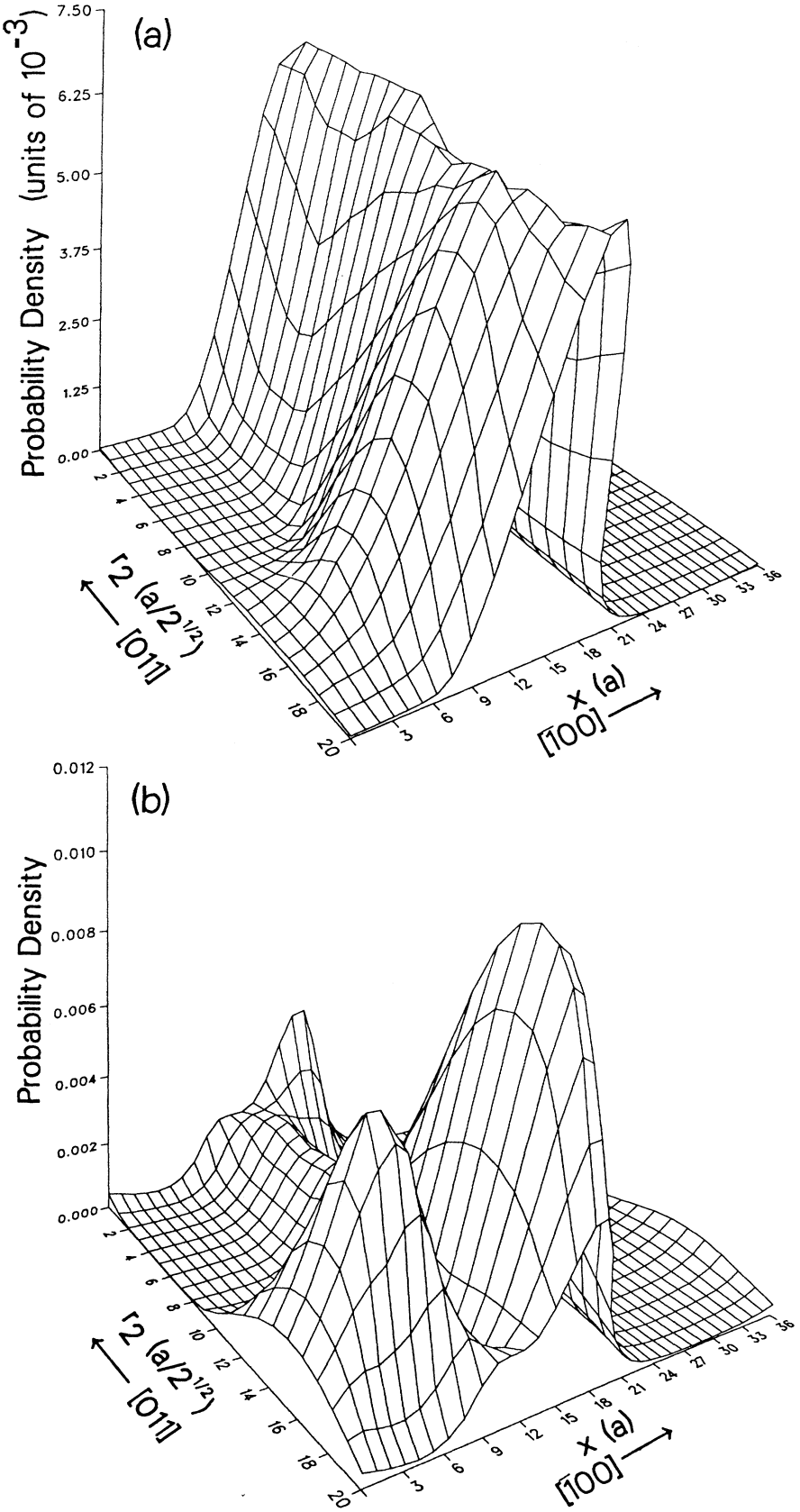

FIG. 5. Probability density plotted within the QWR supercell of the state at (a) the zone center and (b) at the minizone boundary ($k_1=0, k_2=\pi/L_2$) for the first pair of valence subbands (1hh) for the QWR array with parameters used for Fig. 2.

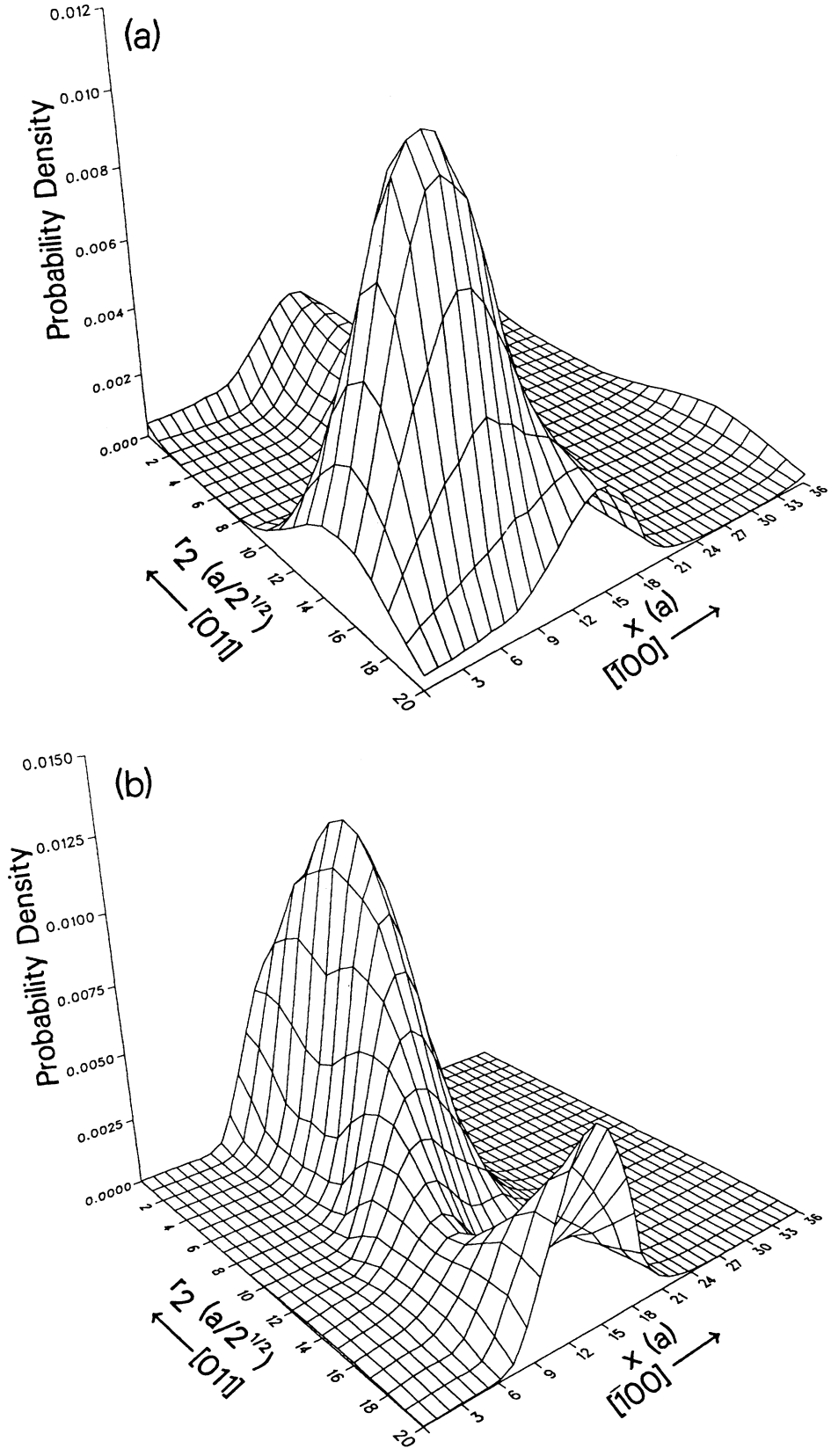

FIG. 6. Probability density plotted within the QWR supercell of the state at (a) the zone center and (b) at the minizone boundary ($k_1=0, k_2=\pi/L_2$) for the second pair of valence subbands (1lh) for the QWR array with parameters used for Fig. 2.

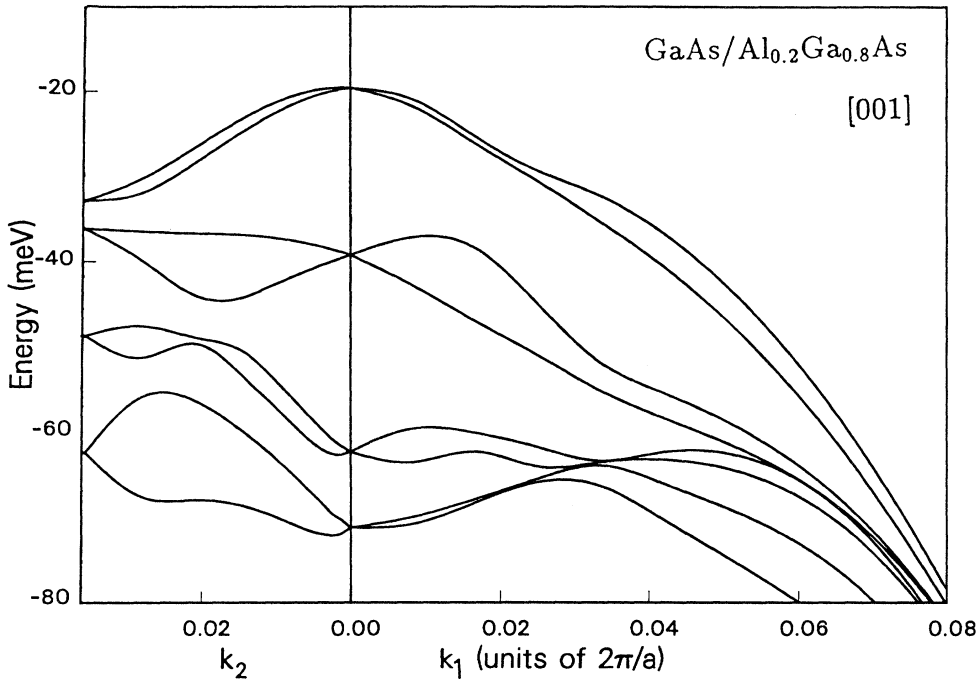

FIG. 7. Valence-subband dispersion in the r_2 and r_1 directions for the structure similar to the one illustrated in Fig. 1 with perfect lateral interfaces but with the QWR axis in the [001] direction. $L_1^W = L_1^B = 50$ Å, $L_2^W = L_2^B = 40$ Å. Energies are measured from the bulk GaAs valence-band edge.

larger k_2 and consequently the valence subbands are sensitive to the spherical and axial approximations. We note in passing that the structure treated in Fig. 7 may be realized as proposed in Ref. 19.

Until now we have assumed that the lateral interfaces in the layer of thickness L_1^B are perfectly abrupt. We have seen on the basis of the subband dispersion and the probability density plots that there are significant effects due to lateral confinement. In the remainder of this subsection we investigate the effect of lateral intermixing on the subband structure. In order to account for the lateral intermixing of species in the QWR array, we consider a sinusoidal compositional profile in the lateral direction r_2 for the layer of thickness L_1^B. Writing the composition as a function of r_2 in this layer as $Al_{\xi(r_2)}Ga_{1-\xi(r_2)}As$, $\xi(r_2)$ takes the form

$$\xi(r_2) = \frac{1}{2}\left[1 + \eta \sin\frac{2\pi r_2}{L_2}\right], \tag{5}$$

where $0 \leq \eta \leq 1$. The value of η for MBE-grown structures is thought to lie approximately in the range $0.15 \leq \eta \leq 0.3$ (Ref. 25). MOCVD-grown QWR arrays may have better lateral definition.[25] The form for ξ has the virtue of facilitating the evaluation of the matrix elements of the QWR Hamiltonian in the basis of SL states. As the exact form of the lateral modulation of the composition is not precisely known, we work with the convenient expression ξ for the lateral compositional modulation. In Sec. III B we present polarization-dependent optical matrix elements for the cases of $\eta = 0.3$ and 1 as well as for the ideal case in which the lateral interfaces are perfectly abrupt. The lateral modulation in the composition is easily incorporated into our model by means of the virtual-crystal approximation. The bond-orbital parameters at position r_2 are obtained by linear interpolation between those of the pure materials. Thus, our model for lateral diffusion includes the variation of all the band parameters and not just the band offsets. For the cases involving lateral intermixing we calculate the sum in the r_2 direction in the matrix elements of the Hamiltonian in the SL basis[12] assuming the lattice constant in the lateral direction is zero. This allows us to replace the summation by an integration over r_2. The results at the Γ point are unchanged by this procedure.

Before embarking on a discussion of the numerical results, some useful information about the QWR array can be learned from simple considerations. Based on elementary considerations, we show that the realistic QWR array in which there is considerable lateral intermixing is less effective than the ideal structure in producing effects due to the lateral compositional modulation. Furthermore, we show that the lh is most susceptible to the effects of a laterally modulated layer.

Consider the extreme case of $\eta = 1$. In this case the minimum band offset between the modulated and nonmodulated layers is zero. The dominant effect to be considered is the lateral confining potential in the modulated layer. In order to estimate the energy associated with the lateral confinement, consider a parabolic QW in which the curvature is given by the curvature of $\sin(2\pi r_2/L_2)$ at its minimum. The Hamiltonian then for a one-band

model is

$$H=-\frac{\hbar^2}{2m^*}\nabla^2+\frac{1.155Q}{2}\left[\frac{2\pi r_2}{L_2}\right]^2, \quad (6)$$

where $Q=0.31$ for holes and 0.69 for electrons is the offset in the respective band and units of energy are eV. The mismatch in the band gaps between GaAs and the alloy $Al_\xi Ga_{1-\xi}As$ is $1.155\xi+0.37\xi^2$ measured in eV. In the Hamiltonian we have neglected the bowing of the band-gap mismatch as it introduces only a small anharmonicity which increases the energies. We assume no in-plane motion of the carriers. The energies associated with this Hamiltonian are $E_n=(n+1/2)\hbar\omega_0$ where

$$\omega_0=(1.155Q/m^*)^{1/2}2\pi/L_2$$
$$=1.8\times10^{14}\,\mathrm{s}^{-1}(Qm_e/m^*)^{1/2}\,.$$

The effective masses in the [011] direction for the asymmetric 50-Å QW are $0.074m_e$ and $0.21m_e$ for the 1e and 1hh subbands at the center of the Brillouin zone. The zone-center effective mass for 1lh is large and difficult to calculate from the subband structure. Substituting the in-plane effective masses for the 50-Å QW, we find that the lowest confinement energies E_0 for the electron and hh are 357 and 142 meV, respectively. These confinement energies are considerably higher than the corresponding ones for the QW (81 and 45 meV). This indicates that the electrons and hh's would preferentially reside in the nonmodulated layer as the energy cost to penetrate into the modulated layer is high. Thus, when lateral intermixing is taken into account, based on these simple considerations, we do not expect the laterally modulated layer to have a strong effect on the electrons and hh's. In the case of no lateral intermixing, we model the lateral confinement by a 40-Å-wide infinite potential well. The lowest confinement energies E_0 are now 317 and 112 meV for the electron and hh. These energies are slightly closer to the corresponding energies in the 50-Å QW, and consequently we expect the penetration into the modulated layer to be stronger. For the realistic case of $\eta=0.3$, the argument against carrier penetration into the modulated layer is even stronger but now the band-gap mismatch (a function of r_2) plays the leading role in the exclusion.

Because we do not have a value for the lh effective mass to substitute into the models (the 1lh subband is flat near the Γ point which leads to large errors in the determination of its effective mass), it is difficult to conclude what is the result of lateral intermixing based on these simple considerations. What is clear, however, is that in the case of the parabolic potential well, the confinement energy E_0 goes as $m^{*-1/2}$ while for the square well it goes as m^{*-1}. Thus for a large lh effective mass, the confinement energy for the square well is smaller and closer to the 1lh energy in the 50-Å QW than for the parabolic case. Consequently, we expect that the QWR array without lateral intermixing is more effective in laterally confining the lh than the QWR array with lateral intermixing. These expectations are borne out in the calculations discussed in the following paragraphs.

Finally, in order to test our model for lateral intermixing against a situation for which there exist both experimental data and theoretical calculations, we consider the QWR arrays of Ref. 30 (see also Ref. 31 for a similar study). In that study QWR arrays like that depicted in Fig. 1 with $L_2^B=L_2^W$ for various values of L_2 were studied. In these structures $L_\perp^B=60$ Å and $L_\perp^W=28$ Å. The barrier material is all $Al_{0.5}Ga_{0.5}As$ and the well material is GaAs. In Fig. 5 of Ref. 30 are plotted experimental data for PL peak wavelength as a function of the lateral period L_2 together with theoretical calculations of the interband energy in which the effect of lateral diffusion is included. In Fig. 8 are plotted our results for the interband transition energy (given in terms of wavelength) as a function of L_2 for the cases of no lateral intermixing and of lateral intermixing with $\eta=1$ for the structures of Ref. 30. The experimental data of Ref. 30 are shown as circles. Overall agreement with the experimental data is obtained for tilt angles greater than 2° ($L_2<80$ Å). This must be qualified with the statement that excitonic effects have not been included. Assuming excitonic binding energies of ~10 meV, the curves in Fig. 8 should be moved upward by ~5 nm. For larger lateral periods, finite migration lengths during growth might limit the applicability of our model. This aside, we expect that as the tilt angle goes to zero (L_2 goes to infinity) the confinement energies should be characteristic of a $L_\perp=90$ Å QW. In the opposite limit of large tilt angle (small L_2), we expect the confinement to be that of an asymmetric QW of width

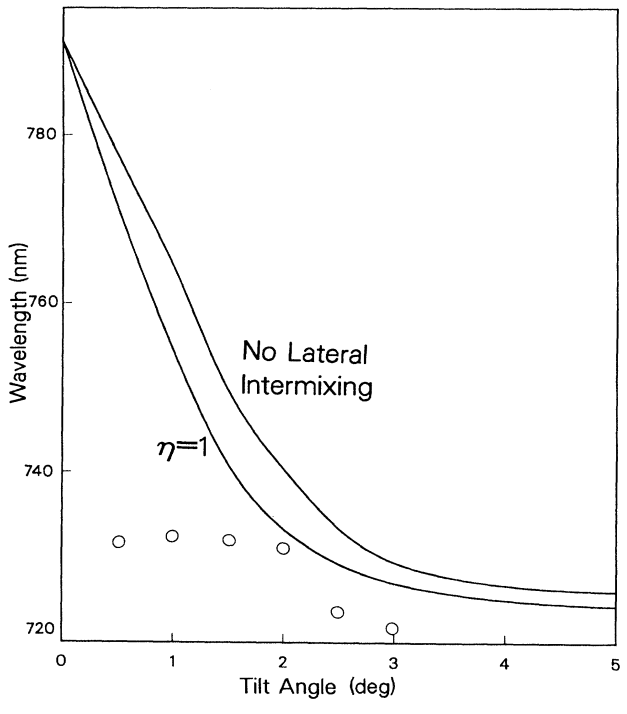

FIG. 8. Interband transition energy (given as a wavelength) for the structures grown in Ref. 26 with $L_\perp^B=60$ Å and $L_\perp^W=30$ Å. (We use $L_\perp^W=28$ Å for our calculations in order to have an integral number of bilayers.) The circles are the experimental data points shown in Fig. 5 of Ref. 26. The tilt angle α is related to the lateral period by $L_2/a=\cot\alpha$.

$L_{\perp}^{W}=28$ Å. (The wavelength of the first PL peak would be 724 nm, neglecting excitons.) But in this limit the steps themselves become important and these have been neglected in our calculations.

Having demonstrated the appropriateness of our method, we proceed to discuss our results. Characterization studies of structures like the QWR array of Ref. 2 indicate that the modulation in the composition is given approximately by ξ with $0.15<\eta<0.3$. For these values of η it was found that the QWR subbands near the band edge coincide with the QW dispersion. In order to magnify the effects of confinement, we choose $\eta=1$. In Fig. 9 is shown the valence-subband dispersion of this structure. The first conduction subband (not shown in the figure) is at 1603 meV and has the zone-center effective mass of $0.075m_e$ in the k_1 direction and $0.080m_e$ in the k_2 direction. These values are virtually identical with the effective masses for the QWR array without lateral intermixing and very close to those for the asymmetric 50-Å QW and the QWR array with no lateral intermixing.

Several features in Fig. 9 are in marked contrast with Fig. 2. In Fig. 9 we see that the position of the 1lh subband is depressed with respect to the corresponding subbands in Fig. 2. This gives a subband spacing of 20 meV between the first and second pair of valence subbands. This is closer to the $1e$-1hh–$1e$-1lh peak spacing in the PLE data of Ref. 2. There is little flattening of the subbands and the minigaps are small. The severe subband repulsions are a consequence of the high degree to which zone folding accounts for all of the subbands. On the basis of Fig. 9 we expect little effect due to lateral confinement for the case of $\eta=1$ and consequently for $\eta=0.3$. Thus, the simple one-band model discussed above led qualitatively to the same conclusion as the detailed numerical model.

Some of the results of this section have been anticipated by the conduction-subband calculations which have recently appeared in Ref. 32 for similar, though modulation-doped, QWR arrays. In that reference, coupled Poisson and Schrödinger equations for the electrons were solved using a finite-element technique. Conduction-subband dispersion in the lateral k_2 direction and charge densities were calculated. Because the structures treated in this study differ from those of Ref. 2, a detailed comparison of the results is made difficult. Nevertheless, we can make the following brief observations. In Ref. 32 the dispersion in the lateral direction was found to be largely explainable in terms of zone folding with the introduction of minigaps similar to what is shown in Fig. 3 of this paper. Also, charge densities for different states showed various degrees of quasi-two-dimensional confinement (see Figs. 4–6 of this study).

B. Optical matrix elements

In this subsection we present results for optical matrix elements calculated within EBOM. In particular we are interested in the polarization dependence of the optical

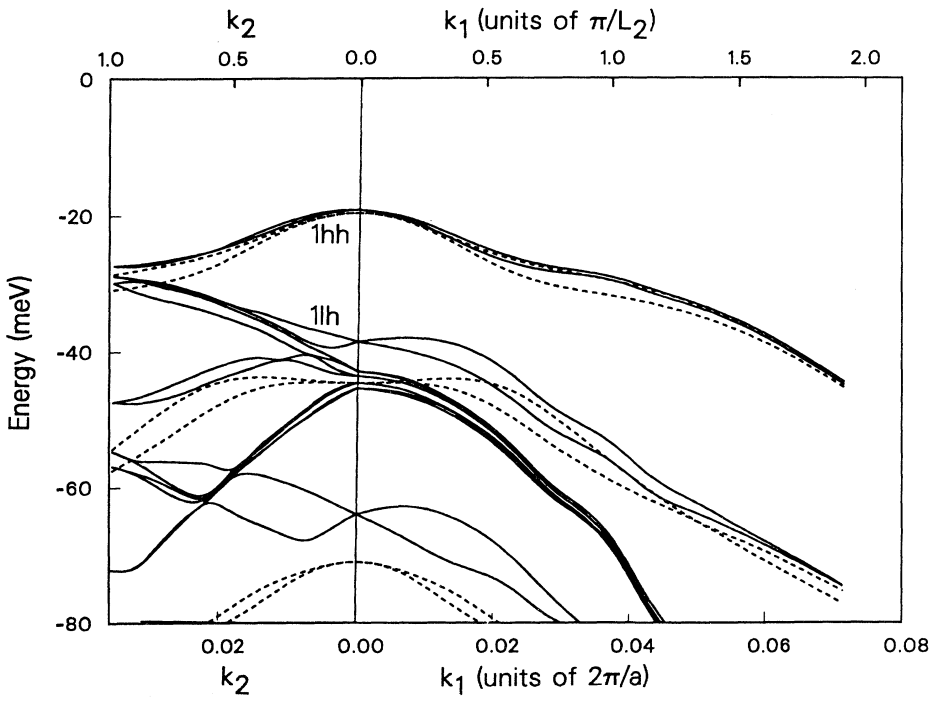

FIG. 9. Valence-subband dispersion (solid curves) in the r_2 and r_1 directions for the structure illustrated in Fig. 1 with lateral compositional modulation in layer of thickness $L_{\perp}^{B}$ given by $\eta=1$. $L_{\perp}^{W}=L_{\perp}^{B}=50$ Å, $L_{2}^{W}=L_{2}^{B}=40$ Å. Dashed curves show valence-subband dispersion for a 50-Å $Al_{0.5}Ga_{0.5}As/GaAs/Al_{0.2}Ga_{0.8}As$ quantum well. Energies are measured from the bulk GaAs valence-band edge.

matrix elements. The optical matrix elements together with the subband structure calculated in the previous subsection provide the essential ingredients from which we calculate the strengths of excitonic transitions. Because the QWR array shares characteristics both of one- and of two-dimensional systems, direct computations of excitonic oscillator strengths and PLE spectra are prohibitively long. We do, however, propose below a simple model for the optical properties which captures the essential physics.

Squared optical matrix elements calculated in EBOM (Ref. 16) as a function of k_1 are plotted in Fig. 10 for polarization parallel (solid curves) and perpendicular (dashed curves) to the QWR's, respectively, for atomically sharp lateral interfaces and in Fig. 11 for the case treated in Fig. 9 ($\eta=1$). The transitions considered are 1e-1hh and 1e-1lh. These curves were obtained by summing the contributions due to subbands degenerate at the Γ point. Focusing on the case of well-defined lateral interfaces (Fig. 10), for the parallel polarization, the largest squared optical matrix element at the zone center is for the 1e-1hh transition. The 1e-1lh transition is considerably weaker for light polarized in the k_2 direction. Comparison of the two polarizations shows strong optical anisotropy with the 1e-1hh transition stronger for the parallel polarization and the 1e-1lh transition stronger for the perpendicular polarization. The squared optical matrix elements at the Γ point for the 1e-1hh and the 1e-1lh transitions are given in Table IV.

The case of lateral intermixing is shown in Fig. 11. Interchanging k_1 and k_2 in Fig. 11 results in similar curves illustrating the weak optical anisotropy. Thus the squared optical matrix elements are considerably more isotropic than for the ideal case. For $\eta=0.3$ the anisotropy is negligible and we do not include plots for this case. The case of $\eta=1$, it should be reiterated, corresponds to a structure with lateral definition considerably better than thought to be the case for the real structure ($0.15<\eta<0.3$).[25] The zone-center values for $\eta=1$ and 0.3 are also included in Table IV. The values for the 1e-1hh transition for the parallel polarization exceed the bulk value against expectation. This is due to the mixing into the zone center of states of nonzero k_2 which may have squared optical matrix elements greater than the zone-center bulk value (see Figs. 10 and 11). The effect is not large and it may be exaggerated by EBOM.

The remainder of this section is concerned with a comparison of the PLE data[2] and the theoretical calculations of this study. Neglecting an occupancy factor, the expression for PLE is quite similar to that for optical absorption. Thus we expect that the absorption spectra contains all the salient features of the PLE data. Apart from a constant factor, the excitonic absorption is given by

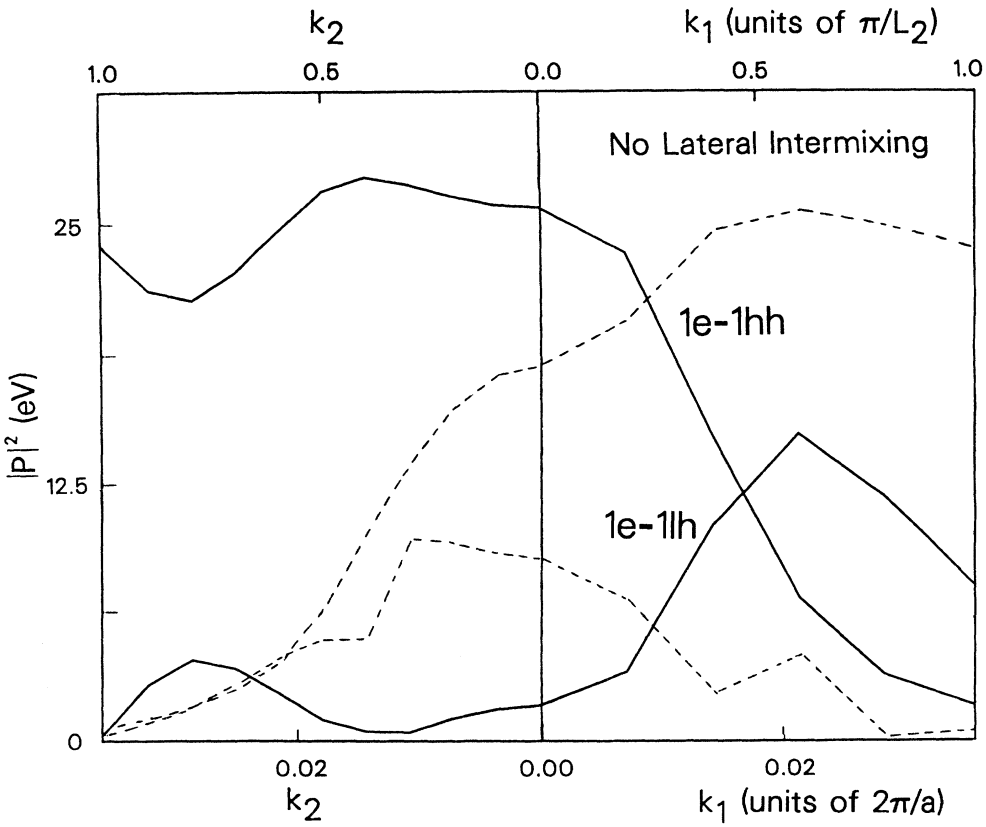

FIG. 10. Squared optical matrix elements in eV for transitions from 1hh and 1lh to 1e for light polarized parallel (solid curves) and perpendicular (dashed curves) to the QWR axis for the case of no lateral intermixing. The curves are labeled as pairs in order from the valence-band edge.

TABLE IV. Squared optical matrix elements at the zone center in eV for light polarized parallel and perpendicular to the QWR axis.

Transition	Polarization	No lateral intermixing	$\lvert\hat{\epsilon}\cdot\mathbf{P}_{1,n}(0,0)\rvert^2$ $\eta=1$	$\eta=0.3$
1ehh	∥	26.3	23.8	23.1
1elh	∥	1.9	5.6	8.1
1ehh	⊥	18.1	21.9	23.1
1elh	⊥	8.8	6.9	8.1

$$\alpha^{\mathrm{ex}}_{1e\text{-}1\mathrm{hh}}(\omega)\sim\frac{1}{L^{W}_{\perp}\omega}|\Phi_{1e\text{-}1\mathrm{hh}}(r=0)|^2|\hat{\epsilon}\cdot\mathbf{P}_{1e,1\mathrm{hh}}(0,0)|^2 \times\frac{\Gamma_{1e\text{-}1\mathrm{hh}}}{\pi}\{[\omega-E^{e}_{1}(0,0)+E^{h}_{1\mathrm{hh}}(0,0)+E^{\mathrm{ex}}_{1e\text{-}1\mathrm{hh}}]^2+\Gamma^2_{1e\text{-}1\mathrm{hh}}\}^{-1}, \quad (7)$$

where $\Gamma_{1e\text{-}1\mathrm{hh}}$ is the half width of the $1e$-1hh excitonic peak in the spectrum and $E^{\mathrm{ex}}_{1e\text{-}1\mathrm{hh}}$ is the binding energy for the $1e$-1hh exciton. A similar expression holds for the $1e$-1lh transition. In order to obtain this expression, we have assumed that the spatial extent of the excitonic envelope function is sufficiently large so that only the optical matrix elements in a region of k space close to the zone center contribute. Consider an envelope function of the form

$$\Phi_n(r)=(2/\pi)^{1/2}(2/a_n)\exp(-2r/a_n),$$

where the Bohr radius is $a_n=4\pi\epsilon_0\hbar_2/(\mu_n e^2)$ with $n\in\{1e\text{-}1\mathrm{hh},\ 1e\text{-}1\mathrm{lh}\}$. The two-dimensional expression is justified since, although the hole experiences significant lateral confinement, the electron does not. Because the electron effective mass is about an order of magnitude lower than the hole effective mass for these subbands, we expect the electron properties to dominate over the hole properties in the determination of the excitonic binding energy and envelope function. The ratio of the height of the n PLE peak for the m polarization to the n' peak for the m' polarization is then

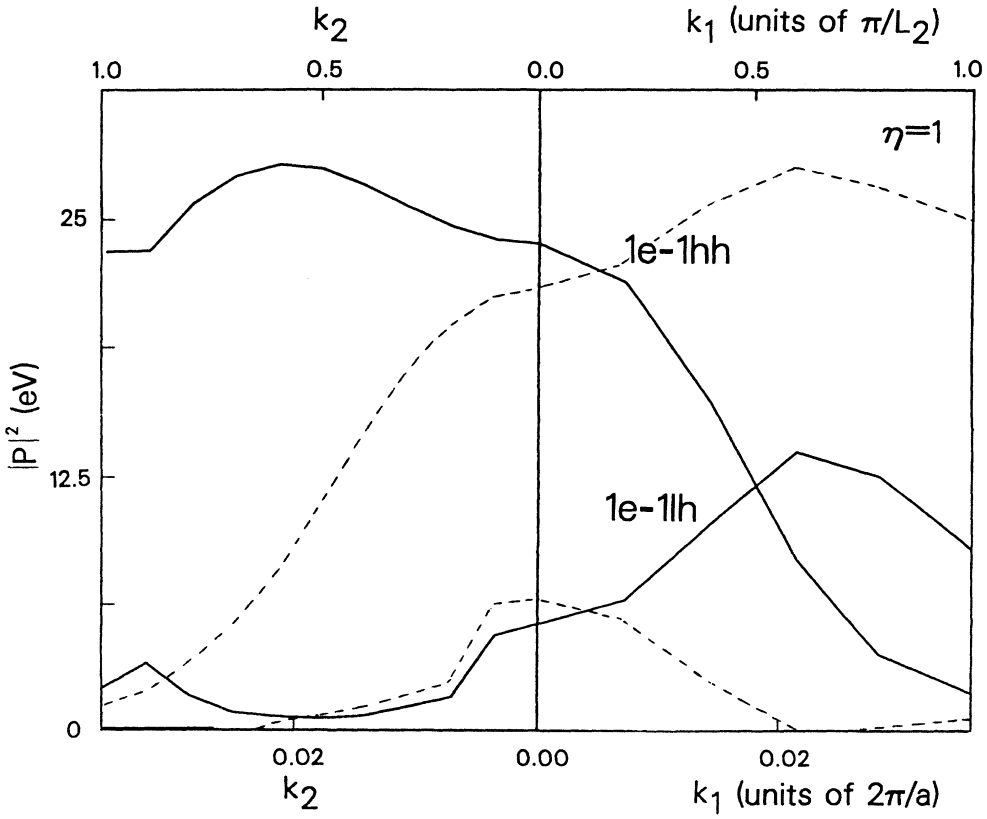

FIG. 11. Squared optical matrix elements in eV for transitions from 1hh and 1lh to $1e$ for light polarized parallel (solid curves) and perpendicular (dashed curves) to the QWR axis for the case of lateral intermixing given by ξ and $\eta=1$. The curves are labeled as pairs in order from the valence-band edge.

$$\left[\frac{\mu_n}{\Gamma_n}|\hat{\epsilon}_m\cdot\mathbf{P}_n(0,0)|^2\right]\Big/\left[\frac{\mu_{n'}}{\Gamma_{n'}}|\hat{\epsilon}_{m'}\cdot\mathbf{P}_{n'}(0,0)|^2\right] . \quad (8)$$

The reduced effective masses for the 1e-1hh and 1e-1lh excitons are approximately the same and are neglected. The half-widths of the 1e-1lh peak is difficult to determine from the experimental spectra, and we shall ignore the factors involving Γ_n and consider the optical anisotropy for a fixed peak given by

$$|\hat{\epsilon}_m\cdot\mathbf{P}_n(0,0)|^2/|\hat{\epsilon}_{m'}\cdot\mathbf{P}_n(0,0)|^2 ,$$

where the squared optical matrix elements are given in Table IV. For the case of no lateral intermixing, the ratio of the peak heights for the 1e-1hh transition for the parallel to the perpendicular polarization is 1.4 while for the 1e-1lh transition the ratio is 0.2. This is in rough agreement with the observed ratios which are ~ 2 and ~ 0.5, respectively. For $\eta=1$ the anisotropy is weak and for $\eta=0.3$, which is believed to apply to the actual structure, the anisotropy is negligible.

The data in Table IV give approximately the maximum rise in PL efficiency of the QWR array with respect to the asymmetric QW. As we argued, the major modification to the 1e-1hh peak brought about by the lateral modulation is due to the oscillator strength. Thus, for the QWR array under consideration we expect a maximum enhancement in the PL efficiency of about 26.3:23.1=1.1 or about 10% with respect to the asymmetric QW (essentially $\eta=0.3$). This enhancement is due solely to the mixing of a light-hole contribution into the 1hh state at the zone center. This assumes perfect lateral interfaces and is for the parallel polarization. We reiterate that this value might be exaggerated as a result of our computational technique. Some of these results are discussed in Ref. 33.

IV. RELATED STRUCTURES

The QWR array of Ref. 2 clearly involves one of many possible choices of the parameters $L_\perp$, $L_\perp^B$, and L_2^B. It is of interest to see how the subband structure varies with these parameters. It is also of interest to see if there is a smooth or sharp transition between one- and two-dimensional subband structure as the parameters are varied. A related question concerns whether this crossover is the same for electrons and holes.

In this section we investigate the zone-center energy levels as a function of the height $L_\perp^B$ and the width L_2^B of the AlAs barriers. The period L_2 in the r_2 direction is kept fixed at 80 Å because most of the published data for tilted SL's grown to data are on 2° viscinal substrates. This gives an average spacing of 80 Å between monolayer steps. We also keep $L_\perp$ fixed at 100 Å.

In Fig. 12 are plotted the energies for the first two pairs of conduction and valence subbands at the center of the Brillouin zone as a function of $L_\perp^B$ for various values of L_2^B. The limiting cases are for the $L_2^B=0$ and 80 Å. These represent 100 Å/300 Å GaAs/$Al_{0.2}Ga_{0.8}As$ and (100 Å$-L_\perp^B$)/$L_\perp^B$/300 Å GaAs/AlAs/$Al_{0.2}Ga_{0.8}As$ SL's, respectively. These calculations are exact in EBOM with $s=2$. For the latter case as $L_\perp^B$ goes to 100 Å, the states become confined in the $Al_{0.2}Ga_{0.8}As$ with a SL energy gap of 1.775 eV. The energy gap of $Al_{0.2}Ga_{0.8}As$ is given in Table I as 1.7635 eV. The discrepancy of 12 meV between the energy gaps of the SL and bulk $Al_{0.2}Ga_{0.8}As$ is due to residual confinement energy in the 300-Å $Al_{0.2}Ga_{0.8}As$ layer. Thus, in the range of high $L_\perp^B$ and L_2^B the carriers are effectively squeezed out of the GaAs and in the limit of infinitely thick $Al_{0.2}Ga_{0.8}As$ layers are no

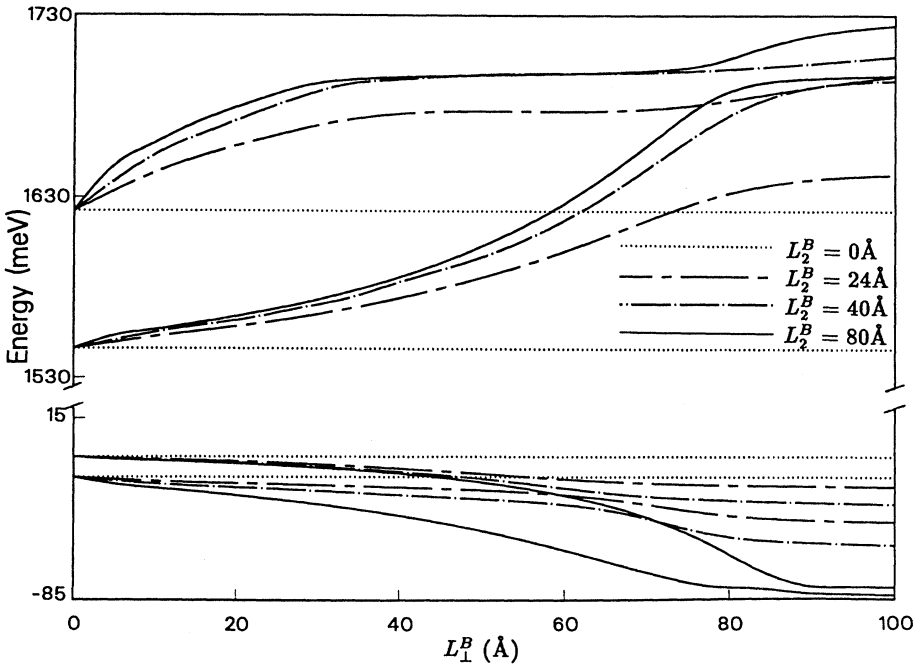

FIG. 12. Zone-center energies of the first two conduction and valence subbands as a function of $L_\perp^B$ for various values of L_2^B. $L_\perp=100$ Å, $L_2=80$ Å.

longer bound.

For $L_{\perp}^{B} \sim 80$ Å for electrons and ~ 90 Å for holes there is a sharp change in behavior for the GaAs/AlAs/$Al_{0.2}Ga_{0.8}As$ SL. In this region the carriers become confined in the $Al_{0.2}Ga_{0.8}As$ layer. In this region we expect the structure to go over to type-II (spatially indirect) behavior. This effect is well known from work on asymmetric QW's.[35–37] In the case shown in Fig. 12, however, the spatially indirect nature is due to the electron becoming unbound while the hole remains confined in the GaAs well material. In Ref. 35, the type-II behavior is associated with confining the electron and hole in separate, though coupled, QW's. For the QWR arrays, in the corresponding regions the QWR's in the array become more weakly coupled and strong hh-lh mixing takes place. For $L_{\perp}^{B}$ thick but L_{2}^{B} thin, the carriers are strongly confined in the GaAs and the subband spacing is characteristic of QWR subband structure. (Compare hole energies of Fig. 12 for $L_{2}^{B}=24$ Å at $L_{\perp}^{B}=100$ Å with the zone-center energies of the upper two subbands in Fig. 2 of Ref. 10.) For $L_{\perp}^{B}$ thick and L_{2}^{B} thick, the carriers penetrate into the $Al_{0.2}Ga_{0.8}As$ layers but are still bound in the GaAs regions. The subband energies for the QWR arrays are bounded by the corresponding curves for the two SL's. In order to form type-II QWR arrays, very thin ($L_{2}^{W} \sim 15$ Å) QWR's are necessary. It may be possible through careful engineering of the dimensions of the QWR array to exploit the crossover between type-I and -II behavior.

Similar structures are proposed and investigated theoretically in Ref. 19. In that work, quasi-two-dimensional confinement is to be achieved by growing a QW on the cleaved edge of a SL. Because of the differences in the details of the structure and the simplifications made in the calculations in Ref. 19, an exact agreement between our results and those of the earlier investigation are not to be expected; however, it is still meaningful to make a comparison for electrons as we found that the 1*e* subband was virtually identical for the cases where the QWR axis lies in the $[0\bar{1}1]$ and [001] directions. For the case of $L_{\perp}^{B}=60$ Å, $L_{2}^{B}=40$ Å in Fig. 12, the confinement energy for the zone-center state for the first conduction subband is ~ 100 meV. In Fig. 2 of Ref. 19, for $d_0=d_1=40$ Å, the confinement energy is ~ 125 meV. In Ref. 19 the flat interface between the well and barrier material (regions II and III in Fig. 1 of Ref. 19) is GaAs/AlAs. Thus the carrier penetration into region III is small and is consequently strongly influenced by the modulation in the band offsets in region I. The charge distribution is more one-dimensional and hence the confinement energy is higher than the structure fabricated in Ref. 2 and the structures treated in this study.

Previously we mentioned that the period in the r_2 direction of similar QWR arrays may vary between 65 and 110 Å. Then for the QWR array of Ref. 2, assuming that the AlAs barriers themselves are of constant width, this means that L_{2}^{W} may vary between 25 and 70 Å.[27] If Fig. 12 is to some degree applicable in these cases, the spreads in the energies of the 1*e*-1hh and 1*e*-1lh transitions $L_{\perp}^{B}=50$ Å for the case treated is approximately 10 and 20 meV respectively. The full width at half-maximum (FWHM) of the 1ehh peak in Ref. 2 is given to be 7.7 meV. The FWHM of the 1elh peak appears to be more than twice that value. These peak widths are in keeping with the deviation from periodicity in the QWR sizes observed in Ref. 25. This in itself, however, does not account for the discrepancies between the calculated energies of the 1*e*-1hh and 1*e*-1lh transitions and the positions of the 1ehh and 1elh peaks.

Another class of nanostructures are the laterally strained structures of Ref. 38. In that work, a GaAs/$Al_xGa_{1-x}As$ QW was grown on the cleaved edge of a GaAs/$In_xGa_{1-x}As$ strained-layer SL. It was hoped that the lateral strain in the edge-grown QW would induce lateral confinement of the carriers. Polarization dependence in the PLE spectra is observed and follows the trends observed in Refs. 2 and 3. Unfortunately, as the strain field in the material is not known in detail, it is difficult to discuss the data in the light of our calculations. It is not clear, for example, whether the polarization dependence might be due to the anisotropic strain itself, rather than due to lateral confinement, nor is it obvious that the strain field is appreciable in the QW.

Other classes of structures exhibiting lateral confinement are strain confined structures[39] by means of stressors and ion-implanted structures.[40–42] EBOM already has been applied successfully to strained-layer SL's. The application of the formalism to situations in which lateral confinement is achieved by strain is straightforward though has not been carried out yet. In ion-implanted structures there may be considerable damage to bombarded regions. We have, therefore, opted to treat expitaxially grown structures.

V. CONCLUSIONS

EBOM is a highly flexible formalism well suited to calculating subband structure and matrix elements for realistic nanostructures and has proven accurate in calculating subband structures for SL's,[13] strained QW's,[43] energy levels of semiconductor quantum dots,[15] and impurity levels in quantum dots[15] and QW's.[44] In this study, we have demonstrated the utility of EBOM in calculating electronic structure and optical properties for QWR arrays grown on vicinal surfaces. In summary, the structure of Ref. 2 must be understood as a perturbed QW. We find that for the parameters given[2,25] inclusion of the lateral compositional intermixing effectively ecludes the carriers from the layer of thickness $L_{\perp}^{B}$ resulting in a structure of which the predicted properties are close to those of an asymmetric QW. When we considerably underestimate the lateral intermixing ($\eta=1$) the optical anisotropy is still considerably smaller than observed.

ACKNOWLEDGMENTS

This work was supported by the National Science Foundation (NSF) under Grant No. NSF-DMR-89-20538.

[1]E. Kapon, D. M. Hwang, and R. Bhat, Phys. Rev. Lett. **63**, 430 (1989).
[2]M. Tsuchiya, J. M. Gaines, R. H. Yan, R. J. Simes, P. O. Holtz, L. A. Coldren, and P. M. Petroff, Phys. Rev. Lett. **62**, 466 (1989).
[3]M. Tanaka and H. Sakaki, Appl. Phys. Lett. **54**, 1326 (1989).
[4]P. C. Sercel and K. J. Vahala, Appl. Phys. Lett. **57**, 545 (1990).
[5]D. S. Citrin and Y.-C. Chang, Phys. Rev. B **40**, 5507 (1989).
[6]D. S. Citrin and Y.-C. Chang (unpublished).
[7]X. Jianbai and H. Kun, Chin. J. Semicond. **8**, 1062 (1988).
[8]J. A. Brum, G. Bastard, L. L. Chang, and L. Esaki, Superlattices Microstruct. **3**, 47 (1987).
[9]M. Sweeny, J. Xu, and M. Shur, Superlattices Microstruct. **4**, 623 (1988).
[10]J. A. Brum and G. Bastard, Superlattices Microstruct. **4**, 443 (1988).
[11]I. Suemune, L. A. Coldren, and S. W. Corzine, Superlattices Microstruct. **4**, 19 (1988).
[12]D. S. Citrin and Y.-C. Chang, J. Appl. Phys. **68**, 161 (1990).
[13]Y.-C. Chang, Phys. Rev. B **37**, 8215 (1988).
[14]Y. D. Galeuchet, P. Roentgen, and V. Graf, Appl. Phys. Lett. **53**, 2638 (1988); in *Proceedings of the Nato ARW on Science and Engineering of 1- and 0-Dimensional Semiconductors, Cadiz, 1989, NATO Advanced Study Institute* (Plenum, New York, in press).
[15]G. T. Einevoll and Y.-C. Chang, Phys. Rev. B **40**, 9683 (1989).
[16]E. O. Kane, J. Phys. Chem. Solids **1**, 82 (1956).
[17]Y.-C. Chang, J. Cheung, A. Chiou, and M. Khoshnevisan, J. Appl. Phys. **68**, 4233 (1990).
[18]H. Sakaki, K. Wagatsuma, J. Hamasaki, and S. Saito, Thin Solid Films **36**, 497 (1976).
[19]Y.-C. Chang, L. L. Chang, and L. Esaki, Appl. Phys. Lett. **47**, 1324 (1985).
[20]*Numerical Data and Functional Relationships in Science and Technology,* edited by K.-H. Hellwege, Landolt-Börnstein, New Series, Vol. III/17a (Springer, Berlin, 1982).
[21]H. J. Lee, L. Y. Jaravel, J. C. Wooley, and A. J. Springthorpe, Phys. Rev. B **21**, 659 (1980).
[22]R. C. Miller, D. A. Kleinman, and A. C. Gossard, Phys. Rev. B **29**, 7085 (1984).
[23]A. D. Katnani and G. Margaritondo, Phys. Rev. B **28**, 1944 (1983); R. S. Bauer and G. Margaritondo, Phys. Today **40**, (1), 27 (1987).
[24]S. A. Chalmers, A. C. Gossard, A. L. Weisenhorn, S. A. C. Gould, B. Drake, and P. K. Hansa, Appl. Phys. Lett. **55**, 2491 (1989).
[25]S. A. Chambers (private communication).
[26]S. W. Corzine, R. H. Yan, and L. A. Coldren (unpublished).
[27]I. Suemune, L. A. Coldren, and S. W. Corzine, Superlattices Microstruct. **4**, 19 (1988); I. Suemune and L. A. Coldren, IEEE J. Quantum Electron. **QE-24**, 1778 (1988).
[28]For example, we compared with the PLE data for slightly wider, though slightly deeper, quantum wells in Table I of P. Dawson, G. Duggan, H. I. Ralph, K. Woodbridge, and G. W. Hooft, Superlattices Microstruct. **1**, 231 (1985).
[29]See Table II (60:40 band offsets) of D. Ninno, M. A. Gell, and M. Jaros, J. Phys. C **19**, 3845 (1986).
[30]T. Fukui, H. Saito, Y. Tokura, K. Tsubaki, and N. Susa, Surf. Sci. **228**, 20 (1990).
[31]M. Tanaka and H. Sakaki, Jpn. J. Appl. Phys. **27**, L2025 (1988).
[32]Y. Tokura, K. Tsubaki, and N. Susa, Appl. Phys. Lett. **55**, 1403 (1989); Y. Tokura, K. Tsubaki, and N. Susa, Surf. Sci. **228**, 280 (1990).
[33]D. S. Citrin and Y.-C. Chang, J. Appl. Phys. **69**, 2685 (1991).
[34]T. Fukui and H. Saito, Jpn. J. Appl. Phys. **229**, L731 (1990).
[35]J. E. Golub, P. F. Liao, D. J. Eilenberger, J. P. Harbison, F. T. Fiorez, and Y. Prior, Appl. Phys. Lett. **53**, 2584 (1988).
[36]J. W. Little, J. K. Whisnant, R. P. Leavitt, and R. A. Wilson, Appl. Phys. Lett. **51**, 1786 (1987).
[37]H. Q. Le, J. J. Zayhowski, and W. D. Goodhue, Appl. Phys. Lett. **50**, 1518 (1987).
[38]D. Gershoni, J. S. Weiner, S. N. G. Chu, G. A. Baraff, J. M. Vandenberg, L. N. Pfeiffer, K. West, R. A. Logan, and T. Tanbun-Ek, Phys. Rev. Lett. **65**, 1631 (1990).
[39]K. Kash, J. M. Worlock, P. Grabbe, A. Scherer, J. P. Harbison, H. G. Craighead, P. S. D. Lin, and M. D. Sturge (unpublished).
[40]Y. Hirayama, Y. Suzuki, S. Tarucha, and H. Okamoto, Jpn. J. Appl. Phys. **24**, L516 (1985).
[41]Y. Hirayama, S. Tarucha, Y. Suzuki, and H. Okamoto, Phys. Rev. B **37**, 2774 (1988).
[42]H. Leier, A. Forchel, B. E. Maile, and G. Weimann, Microelectron. Eng. **9**, 361 (1989).
[43]M.-P. Houng and Y.-C. Chang, J. Appl. Phys. **65**, 3096 (1989); M.-P. Houng, Superlattices Microstruct. **6**, 421 (1989).
[44]G. T. Einevoll and Y.-C. Chang, Phys. Rev. B **41**, 1447 (1989).